

# Non-localities in nucleon-nucleus potentials

## and their effects in nucleon-nucleus scattering

P. Fraser<sup>1</sup>, K. Amos<sup>1</sup>, S. Karataglidis<sup>2</sup>, L. Canton<sup>3</sup>, G. Pisent<sup>3</sup>, and J. P. Svenne<sup>4</sup>

<sup>1</sup> School of Physics, University of Melbourne, Melbourne, Victoria 3010, Australia

<sup>2</sup> Department of Physics and Electronics, Rhodes University, Grahamstown 6140, South Africa

<sup>3</sup> Istituto Nazionale di Fisica Nucleare, Sezione di Padova,  
e Dipartimento di Fisica dell'Università di Padova, Padova I-35131, Italia

<sup>4</sup> Department of Physics and Astronomy, University of Manitoba,  
and Winnipeg Institute for Theoretical Physics, Winnipeg, Manitoba R3T 2N2, Canada

Received: date / Revised version: date

**Abstract.** Two causes of non-locality inherent in nucleon-nucleus scattering are considered. They are the results of two-nucleon antisymmetry of the projectile with each nucleon in the nucleus and the dynamic polarization potential representation of channel coupling. For energies  $\sim 40 - 300$  MeV, a  $g$ -folding model of the optical potential is used to show the influence of the knock-out process that is a result of the two-nucleon antisymmetry. To explore the dynamic polarization potential caused by channel coupling, a multichannel algebraic scattering model has been used for low-energy scattering.

**PACS.** 24.10.-i Nuclear reactions models and methods – 24.10.Eq Coupled channel and distorted wave methods – 24.10.Ht Optical and diffraction models

## 1 Introduction

Non-locality is omnipresent in modern physics having relevance to a quite diverse array of topics. Examples are the heavy-element abundance patterns in white dwarf stars, the bulk modulus of silicon, the tensionless limit of string theory, non-commutative quantum field theory, image retrieval in scanning probe microscopy, electron crystallography, Bose-Einstein condensates, quantum nanostructures, high Reynolds number flow and optical recognition of musical scores.

In nuclear physics, the nucleon-based structure of the nucleus and the scattering and reactions of a projectile (nucleon or nucleus) with a target nucleus, are complicated many-body problems. They involve non-local interactions, and one of the major sources of non-locality arises from the effects of the Pauli principle. The many-nucleon wave function of the system must be antisymmetric with respect to interchange of all pairs of nucleons. This leads to the interaction of an individual nucleon with the rest of the system (the “optical potential” in the case of scattering) having both direct and exchange (knock-out) components. The exchange components are intrinsically non-local. Because of the short-ranged nature of the strong nucleon-nucleon ( $NN$ ) interaction, the exchange amplitudes have significant magnitudes; ones comparable to direct scattering amplitudes.

In this paper, we deal specifically with non-localities arising in effective interaction methods of modelling elas-

tic nucleon-nucleus ( $NA$ ) scattering. The optical potential resulting from such theories is complex (when there is flux loss from the incident channel), energy dependent, and non-local. These characteristics are due in part to the complex nature of the effective  $NN$  interaction underlying the process being modified from the free  $NN$  force because of the presence of the nuclear medium and from effects of the Pauli principle [1]. A non-local and complex optical potential results also from truncating the Hilbert space [2].

The most common approach to analyze (elastic) scattering data is the phenomenological optical model (OM) in which, usually, the  $NA$  interaction potential is chosen to have Woods-Saxon (WS) form with complex strengths, and central plus spin-orbit terms. Those optical potentials are local in form with the energy dependence of the parameters assumed to account for non-local effects. One exception is the specific energy-independent, non-local potential studied by Perey and Buck [3]. There have been other non-local  $NA$  OM potentials proposed, but those invariably have parameters to be specified in searches for good fits to each specific elastic-scattering data set. Such phenomenological approaches, and particularly wave functions derived therefrom, are not reliable. The actual non-localities resulting from more precise treatment of Pauli principle effects, such as with the exchange (knock-out) amplitudes in scattering, and/or of specific accounting for channel-coupling processes, lead to specific energy depen-

dent non-locality effects that are comparable with the non-exchange amplitudes and/or local form corrections to a local optical potential for the channel-coupling processes. In part, the problems are hidden by parameter adjustments in the approximate models being able to give asymptotic phase shifts which lead to reasonable fits to cross-section and other data. Of course, there are a number of ways to determine a local equivalent potential given a specific non-local one. A review of these forms Chapter 11 in Ref. [1]. The results usually are energy dependent and usually involve differentials. However, to fit data with these potentials still requires determination of the parameter set involved. A significant effect of the violation of the Pauli principle inherent may persist [4]. Nonetheless a major problem with use of any local equivalent form lies with just how large the off-diagonal properties of the non-local optical potentials are and/or how large, and with what interference, are their contributions to scattering.

For different energy regimes, when one seeks to minimize phenomenology, different models of  $NA$  scattering are relevant. At energies greater than the excitation energies of giant resonances in the target, a  $g$ -folding model [1] built upon the Kerman-McManus-Thaler (KMT) theory of scattering [5] define microscopic optical potentials. That approach uses complex, energy- and density-dependent  $NN$  effective interactions. With optical potentials built using the Melbourne force [1] as the effective interaction, nucleon-nucleus scattering over the entire mass range and for energies  $\sim 40$  to over 200 MeV has been analyzed successfully [1]. In the regime of energies coinciding with the excitation values of giant resonances, one needs consider their virtual excitation at least as a second-order exchange process [6]. However, at energies from 0 to those for which the giant resonances are expected to be dominant doorway states, and when the target spectrum is discrete, it is more appropriate to use a coupled-channel method to analyze scattering data. That is especially so whenever the discrete spectrum of the target has low-lying collective states. However, most coupled-channel methods of solving  $NA$  scattering problems are based on a collective-model formalism and limited to using local form factors. These methods approximate non-localities with local effects by taking the parameters, used in finding solution of the coupled equations in coordinate space, to be energy dependent. But in so doing the Pauli principle is violated with serious effects [7]. That can be overcome by using the, recently developed [8], multi-channel algebraic scattering (MCAS) scheme; applications of which, even starting with interactions built from the simplest, local form, collective model descriptions, have been quite successful [4, 8, 9]. This method of solution of coupled-channel scattering problems has a number of salient features, notably:

1. With this method, it is quite straight-forward to define specific radial forms of the  $NA$  optical potentials which account for the effects of all channels considered [10].
2. Pauli exclusion effects can be included even when simple (local) collective models are used to define the initial potential function matrix  $V_{cc'}(r)$ .

3. All sub-threshold (bound) states of the compound system can be defined;
4. There is a procedure by which the centroids and widths of all resonances in the scattering can be determined, no matter how narrow any resonance may be.
5. It can be used with any matrix of initial potentials, whether they be local or non-local in form. The latter will be the case, due to the Pauli principle, when detailed nuclear structure is used to define the initial matrix of interaction potentials.
6.  $S$ -matrices and, in fact, complete off-shell  $T$ -matrices are evaluated; the latter required for analysis of off-shell processes such as bremsstrahlung or nucleon capture reaction cross sections.

In the next section, we present some theoretical considerations, outlining the methods we have used to analyze scattering data and specify the effects of non-locality in the problems. For the case of low-energy scattering, we also identify the non-locality in the optical potential. Then, in Sec. III, we present and discuss results. Finally, in Sec. IV, conclusions are drawn.

## 2 Theory considerations

An elegant formulation of  $NA$  optical potentials, given in the book by Feshbach [2], has an operator specification of the dynamical polarization potential (DPP). The Feshbach formalism uses projection operators that divide the Hilbert space into the channels of a given scattering problem that are to be considered explicitly,  $\mathcal{P}$ , and all other channels,  $\mathcal{Q}$ . Feshbach determined that the Schrödinger equation for scattering took the form

$$\left( E - H_{\mathcal{P}\mathcal{P}} - H_{\mathcal{P}\mathcal{Q}} [E - H_{\mathcal{Q}\mathcal{Q}} + i\epsilon]^{-1} H_{\mathcal{Q}\mathcal{P}} \right) \left| \Psi^{(+)} \right\rangle = 0, \quad (1)$$

where  $H_{\mathcal{P}\mathcal{Q}} \equiv \mathcal{P}H\mathcal{Q}$  and similarly for  $H_{\mathcal{Q}\mathcal{P}}, H_{\mathcal{P}\mathcal{P}}$ , and  $H_{\mathcal{Q}\mathcal{Q}}$ . Thus the DPP, formally, is a projection of  $\mathcal{Q}$  space effects to an effective operator in  $\mathcal{P}$  space, i.e.

$$\Delta U_{\mathcal{P}\mathcal{P}} = H_{\mathcal{P}\mathcal{Q}} [E - H_{\mathcal{Q}\mathcal{Q}} + i\epsilon]^{-1} H_{\mathcal{Q}\mathcal{P}}. \quad (2)$$

We consider the case that  $\mathcal{P}$  projects onto the elastic-scattering channel, then

$$\mathcal{P} = |\Psi_{gs}\rangle \langle \Psi_{gs}|; \quad \mathcal{Q} = \mathbf{1} - |\Psi_{gs}\rangle \langle \Psi_{gs}|; \quad \mathcal{Q} |\Psi_{gs}\rangle = 0, \quad (3)$$

and take as the Hamiltonian,

$$H = H_0 + V + H_A \quad ; \quad H_A |\Phi_j\rangle = e_j |\Phi_j\rangle. \quad (4)$$

$|\Phi_j\rangle$  are the eigenstates of the Hamiltonian for the target nucleus and  $e_j$  are the eigenvalues. Then as only the operator  $V$  connects  $\mathcal{Q}$  and  $\mathcal{P}$  spaces, the DPP is

$$\Delta U_{\mathcal{P}\mathcal{P}} = V_{\mathcal{P}\mathcal{Q}} [E - H_{\mathcal{Q}\mathcal{Q}} + i\epsilon]^{-1} V_{\mathcal{Q}\mathcal{P}}. \quad (5)$$

For simplicity, temporarily, we ignore antisymmetrization between the continuum projectile nucleon and all the

$A$  nucleons of the target [2]. Then the  $(A + 1)$  particle states have the form

$$\begin{aligned} |\Psi_j^+\rangle &= |\chi_j^{(+)}\rangle |\Phi_j\rangle = |\chi_j^+(0)\rangle |\Phi_j(1, \dots, A)\rangle, \\ \mathcal{P} |\Psi_j^+\rangle &= |\Psi_{gs}^+\rangle = |\chi_{gs}^+(0)\rangle |\Phi_{gs}(1, \dots, A)\rangle, \end{aligned} \quad (6)$$

and on taking the target ground-state expectation,

$$\begin{aligned} &\left( E - H_0 - e_{gs} - \langle \Phi_{gs} | V | \Phi_{gs} \rangle \right. \\ &\quad \left. - \langle \Phi_{gs} | V G_{QQ}^{(+)} V | \Phi_{gs} \rangle \right) |\chi_{gs}^+\rangle = 0, \end{aligned} \quad (7)$$

where

$$G_{QQ}^{(+)} = [E - H_{QQ} + i\epsilon]^{-1}. \quad (8)$$

Thus, a structural form for the  $NA$  optical potential is identified by

$$\begin{aligned} U_{OM}(E) &= \langle \Phi_{gs} | V | \Phi_{gs} \rangle + \langle \Phi_{gs} | V G_{QQ}^{(+)} V | \Phi_{gs} \rangle \\ &= \langle \Phi_{gs} | V | \Phi_{gs} \rangle + \Delta U(E). \end{aligned} \quad (9)$$

Here  $\Delta U(E)$  is the DPP which leads to a coordinate space optical potential,

$$U_{OM}(\mathbf{r}, \mathbf{r}'; E) = V_{loc}(\mathbf{r}) \delta(\mathbf{r} - \mathbf{r}') + \Delta U(\mathbf{r}, \mathbf{r}'; E), \quad (10)$$

when a local form ( $V_{loc}$ ) for the elemental ground-state interaction is assumed.

But allowing for the Pauli principle whereby the emergent nucleon may not be that incident on the target makes even the leading term non-local. The Schrödinger equations for the relative motion wave functions thus have the form (with  $\chi^{(+)}(\mathbf{r}) \equiv \chi^{(+)}(\mathbf{r}, E)$ )

$$\left( \frac{\hbar^2}{2\bar{m}} \nabla^2 + E \right) \chi^{(+)}(\mathbf{r}) = \int U_{OM}(\mathbf{r}, \mathbf{r}'; E) \chi^{(+)}(\mathbf{r}') d\mathbf{r}'. \quad (11)$$

Here  $\bar{m}$  is the reduced mass, and the energy scale is taken with  $\epsilon_{gs} = 0$

## 2.1 Low-energy regime and MCAS

For nucleons of up to 5 MeV scattering from light mass targets particularly, cross sections show relatively few (resonance) states which are often widely spaced. Low energies also mean few partial waves are important with the scattering (both factors keep the scale of the problem of using MCAS manageable). Nonetheless, the applicability of MCAS is only limited by the computing power and time available.

The essential input to MCAS is a matrix of potentials that define a specific  $NA$  system. The first operational requirement then is to find the optimal expansion of those potentials in separable form. That expansion is made in terms of sturmian functions [8,10] with the sturmians being generated from the chosen matrix of potentials themselves. Then, with separable interactions,

the Hilbert-Schmidt expansion of amplitudes gives the  $T$ -matrix also in separable form.

The MCAS theory [8] treats coupled-channel scattering in momentum space, giving solutions of Lippmann-Schwinger (LS) integral equations. For each spin parity  $J^\pi$  of a given  $NA$  system, one must consider a set of  $\Gamma$  scattering channels, each with a label  $c$  ( $1 \leq c \leq \Gamma$ ) where each  $c$  identifies a set of quantum numbers (all details have been published [8]). Then, in partial wave form, the coupled LS equations define a multichannel  $T$ -matrix,

$$\begin{aligned} T_{cc'}^{J^\pi}(p, q; E) &= V_{cc'}^{J^\pi}(p, q) \\ &+ \mu \left[ \sum_{c''=1}^{\text{open}} \int_0^\infty V_{cc''}^{J^\pi}(p, x) \frac{x^2}{k_{c''}^2 - x^2 + i\epsilon} T_{c''c'}^{J^\pi}(x, q; E) dx \right. \\ &\quad \left. - \sum_{c''=1}^{\text{closed}} \int_0^\infty V_{cc''}^{J^\pi}(p, x) \frac{x^2}{h_{c''}^2 + x^2} T_{c''c'}^{J^\pi}(x, q; E) dx \right] \end{aligned} \quad (12)$$

where  $\mu = 2\bar{m}/\hbar^2$ . There are two summations as the open and closed channel components have been separated with the wave numbers being  $k_c = \sqrt{\mu(E - \epsilon_c)}$  and  $h_c = \sqrt{\mu(\epsilon_c - E)}$  for  $E > \epsilon_c$  and  $E < \epsilon_c$  respectively.  $\epsilon_c$  is the energy threshold at which channel  $c$  is open. Note that henceforth the  $J^\pi$  superscript is to be understood. Expansion of  $V_{cc'}$  in terms of a finite number of sturmians yields

$$V_{cc'}(p, q) \sim \sum_{n=1}^N \hat{\chi}_{cn}(p) \eta_n^{-1} \hat{\chi}_{c'n}(q), \quad (13)$$

where  $\hat{\chi}_{cn}(p)$  relate to the chosen sturmian functions in momentum space and  $\eta$  are the associated eigenvalues [8, 10].

The Fourier-Bessel transforms of the form factors are  $\chi_{cn}(r)$ . They are also defined in terms of the sturmians ( $\Phi_{cn}(r)$ ) by

$$\chi_{cn}(r) = \sum_{c'=1}^{\Gamma} V_{cc'}(r) \Phi_{c'n}(r) \quad (14)$$

if the initial potentials are local in form, and by

$$\chi_{cp}(r) = \sum_{c'=1}^{\Gamma} \int_0^\infty V_{cc'}(r, r') \Phi_{c'p}(r') dr' \quad (15)$$

if those potentials are non-local. It is possible to develop the optical potential in coordinate space with the MCAS theory [8,10]. We will consider only spin zero targets so that the channel indices designate the collected angular momenta  $c \equiv [(l\frac{1}{2})J]$ . Then, for each conserved total angular momentum  $J$  and selected parity, the partial wave  $l$  associated with a zero spin ground state is unique. In the following, the index  $c = 1$  then implies the partial wave specific to each  $J^\pi$  considered.

Assuming a local form for the leading term, MCAS theory gives for the DPP,

$$\Delta U_{1,1}(r, r'; E) = \sum_{c, c'=2}^{\Gamma} V_{1c}(r) G_{cc'}^{(Q)}(r, r'; E) V_{c'1}(r'). \quad (16)$$

The Green's functions are solutions of

$$G_{cc'}^{(Q)} = G_c^{(0)} \delta_{cc'} + \sum_{c''=2}^R G_c^{(0)} V_{cc''} G_{c''c'}^{(Q)}, \quad (17)$$

where  $G_c^{(0)}$  is the free Green's function for each individual channel  $c$ . Historically, finding these solutions has been difficult. However the MCAS development allows the analogous definition [11, 12],

$$\Delta U_{11}(r, r'; E) = \sum_{n, n'=1}^N \chi_{1n}(r) [\mathbf{A}(E)]_{nn'} \chi_{1n'}(r'), \quad (18)$$

where

$$\begin{aligned} \mathbf{A}(E) &= \left[ \boldsymbol{\eta} - \mathbf{G}_0^{(Q)}(E) \right]^{-1} - \boldsymbol{\eta}^{-1}, \\ \left[ \mathbf{G}_0^{(Q)}(E) \right]_{nn'} &= \mu \left[ \sum_{c \neq 1}^{\text{open}} \int_0^\infty \frac{\hat{\chi}_{cn}(x) \hat{\chi}_{cn'}(x)}{k_c^2 - x^2 + i\epsilon} x^2 dx \right. \\ &\quad \left. - \sum_{c \neq 1}^{\text{closed}} \int_0^\infty \frac{\hat{\chi}_{cn}(x) \hat{\chi}_{cn'}(x)}{h_c^2 + x^2} x^2 dx \right]. \end{aligned} \quad (19)$$

### 2.1.1 The Perey-Buck (PB) non-local potential

The PB potential [3] has the energy-independent, non-local, form

$$\begin{aligned} U_{OM}^{PB}(\mathbf{r}, \mathbf{r}'; E) &= v\left(\frac{1}{2}|\mathbf{r} + \mathbf{r}'|\right) \frac{1}{[\sqrt{\pi}\beta_{NL}]^3} e^{-\left(\frac{\mathbf{r}-\mathbf{r}'}{\beta_{NL}}\right)^2} \\ &\Rightarrow v(s) \frac{1}{[\sqrt{\pi}\beta_{NL}]^3} e^{-\left(\frac{\mathbf{r}-\mathbf{r}'}{\beta_{NL}}\right)^2}, \end{aligned} \quad (20)$$

where, with  $s = \frac{1}{2}(\mathbf{r} + \mathbf{r}')$ ,

$$v(s) = V_{NL} \left[ 1 + e^{\left(\frac{s-R_{NL}}{a_{NL}}\right)} \right]^{-1}. \quad (21)$$

As shown in the appendix of Ref. [3], this (reduced) form can be expanded in partial waves with radial multipoles being

$$\begin{aligned} \frac{1}{rr'} g_\ell(r, r') &= \frac{2}{\sqrt{\pi}\beta_{NL}^3} v\left(\frac{1}{2}[r + r']\right) \\ &\times e^{-\left[\frac{(r^2 - r'^2)}{\beta_{NL}^2}\right]} i^\ell j_\ell \left(-i \frac{2rr'}{\beta_{NL}^2}\right). \end{aligned} \quad (22)$$

However, there are parameters involved and so this potential is phenomenological. Nonetheless, the parameters of this interaction, intended for use at low energies and with nuclei of medium and heavy mass, were obtained solely by fitting the differential cross sections for 7.0 and 14.5 MeV neutrons elastically scattered from  $^{208}\text{Pb}$ . Those parameter values then were used [3] in analyses of a set of neutron scattering observables for a range of energy, 0.4

to 24.0 MeV, and for a set of targets ranging from  $^{27}\text{Al}$  to  $^{208}\text{Pb}$ . Good agreement was found between results obtained with those parameters and data taken with those targets.

Though the PB interaction was not used for scattering from  $^{12}\text{C}$ , we adopt it in this study to display its non-local features. The PB prescription is energy independent and so the shape of that non-locality is constant. The results may not be the PB potential that gives a best fit to scattering data from  $^{12}\text{C}$ . But as we only seek to make qualitative comparison with the MCAS results it suffices to use the parameter values initially defined [3].

## 2.2 The $g$ -folding model for medium energies

For energies well above the particle-emission threshold and so coinciding with a continuum of states in the target, multi-nucleon scattering reductions of the formal Feshbach theory of scattering are relevant. It is useful to follow the KMT scheme [5] in which it is assumed that only pairwise interactions between the projectile and individual target nucleons are important. With the projectile tagged by the subscript 0, and target nucleons tagged similarly by  $i$ , the essential interaction can be written

$$V = \sum_{i=1}^A v_{0i} = A v_{01}. \quad (23)$$

With whatever is chosen for the free  $NN$  interaction  $v_{01}$ , the KMT theory allows for multiple pairwise interactions so that  $NN$   $t$ -matrices, solutions of  $NN$  LS equations, are required in applications. However, such an approach does not account for the ways in which those interactions are influenced by the nuclear medium in which the two nucleons interact. Experience [1] has shown that the  $NN$   $g$ -matrices, solutions of the Brueckner-Bethe-Goldstone (BBG) equations for infinite nuclear matter [13], can well approximate those (many-body) corrections. Using the  $NN$   $g$ -matrices in a first order KMT approach involves an assumption that the important terms in  $Q$ -space, for the incident energies concerned, are excitations in which a particle is promoted to a state in an infinite-matter system with Fermi momentum related to the density of the nucleus from where it came. Thus, the effective  $NN$  interaction, besides being energy dependent and complex, also is density dependent [1]. The optical potentials that result on folding these interactions with density matrices of the target nucleus, will be both complex and energy-dependent. Further, by virtue of the Pauli principle at least, they are non-local.

The  $g$ -matrices can be used directly within a momentum space formulation of the  $NA$  optical potential [14] or by forming an effective  $NA$  interaction in coordinate space [1]. Our approach is with the latter and requires a mapping of the actual  $NN$   $g$ -matrices into the coordinate space forms usable in the program DWBA98 [15].

In coordinate space, such non-local optical potentials can be written formally

$$U_{OM} = U_{OM}(\mathbf{r}_1, \mathbf{r}_2; E) = U_{OM}^D(\mathbf{r}_1; E) + U_{OM}^{Ex}(\mathbf{r}_1, \mathbf{r}_2; E) \quad (24)$$

where

$$\begin{aligned} U_{OM}^D(\mathbf{r}_1; E) &= \sum_n \zeta_n \delta(\mathbf{r}_1 - \mathbf{r}_2) \int \varphi_n^*(\mathbf{s}) v_D(\mathbf{r}_{1s}) \varphi_n(\mathbf{s}) d^3s \\ &= \delta(\mathbf{r}_1 - \mathbf{r}_2) \int \rho(\mathbf{s}) v_D(\mathbf{r}_{1s}) d^3s \end{aligned} \quad (25)$$

involving then an integration over the nuclear density, and the exchange term which is totally nonlocal,

$$U_{OM}^{Ex}(\mathbf{r}_1, \mathbf{r}_2; E) = \sum_n \zeta_n \varphi_n^*(\mathbf{r}_1) v_{Ex}(\mathbf{r}_{12}) \varphi_n(\mathbf{r}_2). \quad (26)$$

$v_D$ ,  $v_{Ex}$  are combinations of the components of the effective  $NN$  interactions,  $\varphi_n(\mathbf{r})$  are single-nucleon bound states, and  $\zeta_n$  are bound-state shell occupancies. More generally, the latter are one-body density matrix elements (OBDM). It is not easy to specify actual radial values of these non-local potentials for graphing purposes. The program DWBA98 [15] does not form such in evaluation of solutions of the partial wave Schrödinger equations. The operator structure and strong density dependence of the effective interactions deduced from the  $NN$   $g$ -matrices do not lend themselves easily to create multipole expansions needed to specify  $U_{OM}(r_1, r_2)$  for each partial wave. In finding solutions of the integro-differential equations, the program DWBA98 uses expansions involving particle-hole expectation values of the effective interactions [1]. However, the effects of the inherent non-locality are clearly evident from calculated cross sections and spin observables as we show later. They are also important in predictions of cross-section and spin-observable data from inelastic scattering of nucleons from nuclei.

Cross sections for inelastic proton scattering have been evaluated using a microscopic DWA theory of the processes [1]. In that theory, the transition amplitudes for nucleon inelastic scattering from a nuclear target have the form [1] ( $\Psi_{J_i M_i} \equiv \Psi_{J_i M_i}(1 \cdots A)$ )

$$\begin{aligned} \mathcal{T} &= T_{J_f J_i}^{M_f M_i \nu' \nu}(\Omega_{sc}) \\ &= \left\langle \chi_{\nu'}^{(-)}(\mathbf{k}_o 0) \right| \left\langle \Psi_{J_f M_f} \right| A \mathbf{g}_{\text{eff}}(0, 1) \\ &\quad \times \mathcal{A}_{01} \left\{ \left| \chi_{\nu}^{(+)}(\mathbf{k}_i 0) \right\rangle \left| \Psi_{J_i M_i} \right\rangle \right\}, \end{aligned} \quad (27)$$

where  $\Omega_{sc}$  is the scattering angle and  $\mathcal{A}_{01}$  is the two-nucleon state antisymmetrization operator. The nuclear transition is from a state  $|J_i M_i\rangle$  to a state  $|J_f M_f\rangle$  and the projectile has spin projections  $\nu$  before, and  $\nu'$  after, the collision. The incoming and outgoing distorted waves are specified by  $\chi^\pm$  and they have relative momenta of  $\mathbf{k}_i$  and  $\mathbf{k}_o$  respectively. The development proceeds by using a cofactor expansion of the target states,

$$|\Psi_{JM}\rangle = \frac{1}{\sqrt{A}} \sum_{j,m} |\varphi_{jm}(1)\rangle a_{jm}(1) |\Psi_{JM}\rangle, \quad (28)$$

which allows expansion of the scattering amplitudes in the form of weighted two-nucleon elements since  $a_{jm}(1) |\Psi_{JM}\rangle$  in Eq. (28) is independent of coordinate ‘1’. Thus

$$\begin{aligned} \mathcal{T} &= \sum_{j_1, j_2} \left\langle \Psi_{J_f M_f} \right| a_{j_2 m_2}^\dagger(1) a_{j_1 m_1}(1) \left| \Psi_{J_i M_i} \right\rangle \\ &\quad \times \left\langle \chi_{\nu'}^{(-)}(\mathbf{k}_o 0) \right| \left\langle \varphi_{j_2 m_2}(1) \right| \mathbf{g}_{\text{eff}}(0, 1) \\ &\quad \mathcal{A}_{01} \left\{ \left| \chi_{\nu}^{(+)}(\mathbf{k}_i 0) \right\rangle \left| \varphi_{j_1 m_1}(1) \right\rangle \right\} \\ &= \sum_{j_1, j_2, I} \frac{1}{\sqrt{2J_f + 1}} \langle J_i I M_i N | J_f M_f \rangle S_{j_1 j_2 I}^{(J_i \rightarrow J_f)} \\ &\quad \times \sum_{m_1, m_2} (-1)^{(j_1 - m_1)} \langle j_1 j_2 m_1 - m_2 | I - N \rangle \\ &\quad \times \left\langle \chi_{\nu'}^{(-)}(\mathbf{k}_o 0) \right| \left\langle \varphi_{j_2 m_2}(1) \right| \mathbf{g}_{\text{eff}}(0, 1) \\ &\quad \mathcal{A}_{01} \left\{ \left| \chi_{\nu}^{(+)}(\mathbf{k}_i 0) \right\rangle \left| \varphi_{j_1 m_1}(1) \right\rangle \right\}, \end{aligned} \quad (29)$$

where reduction of the structure factor to (transition) OBDM  $(S_{j_1 j_2 I}^{(J_i \rightarrow J_f)})$  for angular momentum transfer values  $I$  is given in detail elsewhere [1].

The effective interactions  $\mathbf{g}_{\text{eff}}(0, 1)$  used in the folding to get the optical potentials have also been used as the transition operators effecting the excitations. As with the generation of the elastic-scattering optical potentials from which the distorted waves are generated, antisymmetry of the projectile with each individual bound nucleon is treated exactly. The associated knock-out (exchange) amplitudes are the non-local effects in inelastic scattering. They contribute importantly to the evaluated scattering cross section, both in magnitude and shape [1].

## 3 Results and Discussion

### 3.1 MCAS and the low-energy regime

In the paper detailing the MCAS method [8] cross sections and spectra from the scattering of neutrons from  $^{12}\text{C}$  for energies to  $\sim 6$  MeV were studied. The coupled-channel starting potentials were defined from a collective model which included quadrupole deformation. The spectrum of the target,  $^{12}\text{C}$ , was truncated to just the lowest three states; the  $0_1^+$  ground state, the  $2^+$  state at 4.43 MeV and the  $0_2^+$  state at 7.96 MeV. We consider those results again in brief as they are the bound and scattering properties that the DPP we form will reproduce when used in a non-local Schrödinger equation.

With parameter values as used previously [8], MCAS calculations gave the energy variation cross section for low energy  $n+^{12}\text{C}$  elastic scattering that is shown by the solid curve in Fig. 1. The filled circles are the data [16, 17]. The compound nucleus sub-threshold (bound) and resonance states that result are compared with the  $^{13}\text{C}$  spectrum therein as well. The comparison of calculated results with data is very good at least to the energy (4.43 MeV) coinciding with excitation of the first  $2^+$  state. It is of note

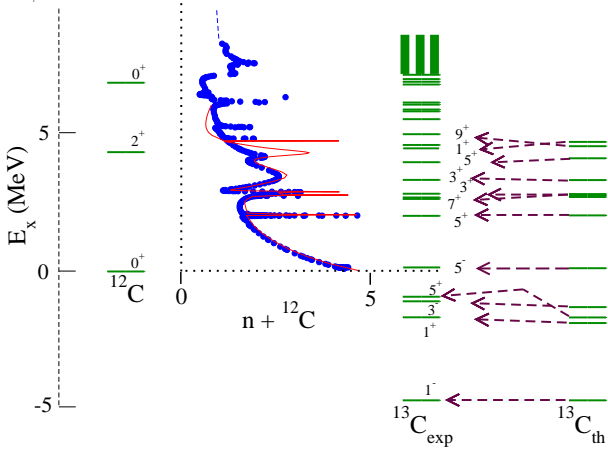


**Fig. 1.** (Color online) MCAS results compared with data from the elastic  $n+^{12}\text{C}$  scattering and with the spectrum of  $^{13}\text{C}$ . Each  $^{13}\text{C}$  state is identified by their parity and twice their spin.

that, using MCAS for the negative (sub-threshold) energy regime gives the correct bound states of  $^{13}\text{C}$ . Accounting for the Pauli principle was crucial to find these results; just how crucial was shown in recent publications [4, 7]. Adding a Coulomb interaction also gave a good spectrum for  $^{13}\text{N}$  and good reproduction of fixed angle, proton elastic-scattering observables [9].

We have evaluated the DPP for this  $n+^{12}\text{C}$  system and results are shown in Fig. 2. Therein the  $0s_{\frac{1}{2}}$ ,  $0p_{\frac{3}{2}}$ , and  $d_{\frac{5}{2}}$  wave DPP values are plotted in the top, middle and bottom segments for energies of 1.5 MeV and of 2.73 MeV in the left and middle panels respectively. The right panel contains some PB potential results that we discuss later. These DPP display a well shape with maximal depths on axis and in the nuclear surface region. The units for these DPP are  $\text{MeV}\cdot\text{fm}^{-1}$  and the  $0s_{\frac{1}{2}}$  wave contours have spacings of  $20 \text{ MeV}\cdot\text{fm}^{-1}$  from a value of  $-20 \text{ MeV}\cdot\text{fm}^{-1}$  with the most outer (dashed) curves. The central well depth of these  $0s_{\frac{1}{2}}$  wave DPP are  $-170 \text{ MeV}\cdot\text{fm}^{-1}$  and  $-240 \text{ MeV}\cdot\text{fm}^{-1}$  for 1.5 MeV and 2.73 MeV neutrons respectively. The  $0p_{\frac{3}{2}}$  and  $0d_{\frac{5}{2}}$  wave DPP respectively are given in contours starting with the outermost value of  $-5 \text{ MeV}\cdot\text{fm}^{-1}$  with  $-5 \text{ MeV}\cdot\text{fm}^{-1}$  steps inward to maximal depth values of  $-22(-23) \text{ MeV}\cdot\text{fm}^{-1}$  and  $-28(-32) \text{ MeV}\cdot\text{fm}^{-1}$  for the incident energy of 1.5 (2.73) MeV. Clearly the DPP are strongly non-local and energy dependent; the  $0s_{\frac{1}{2}}$  wave for this case of  $n-^{12}\text{C}$  scattering particularly so. The  $0p_{\frac{3}{2}}$  and  $0d_{\frac{5}{2}}$  wave forms are not as energy dependent over the 0 to 4 MeV projectile energy range but they, too, are markedly non-local.

Values of DPPs along the diagonal ( $r = r'$ ) are shown in Fig. 3. The  $0s_{\frac{1}{2}}$  and  $0p_{\frac{3}{2}}$  wave DPP diagonal values, shown in the top and in the bottom (left) panels respec-

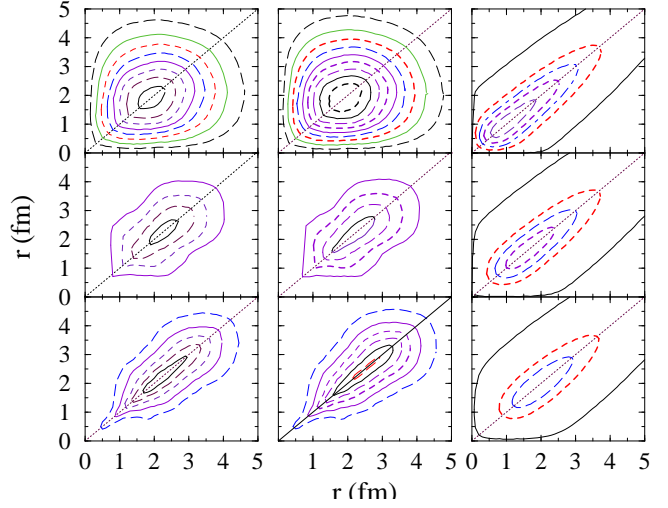


**Fig. 2.** (Color online) Contours of the DPP found using MCAS for neutrons of energies 1.5 MeV (left) and 2.73 MeV (middle) compared with a PB energy-independent form (right).

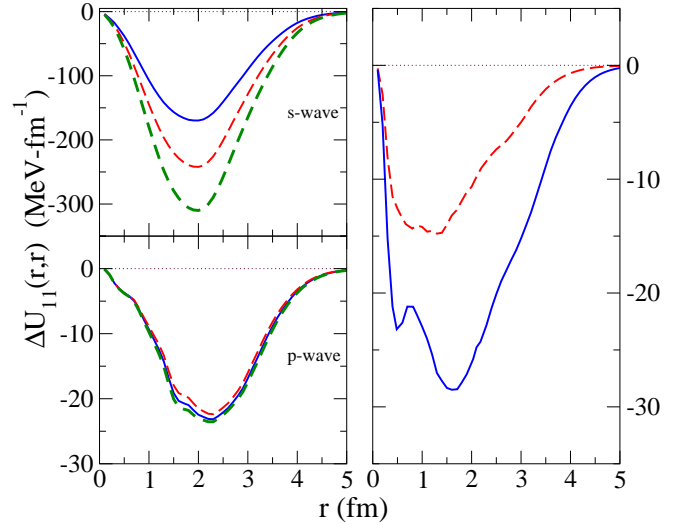


**Fig. 3.** (Color online) The radial variations of the DPP along the diagonal for  $0s_{\frac{1}{2}}$  waves (top left),  $0p_{\frac{3}{2}}$  waves (bottom left) and for  $0d_j$  waves (right). Details are given in the text.

tively, are for incident energies of 1.5 MeV (solid), 2.73 MeV (long dashed), and 3.23 MeV (dashed curves). These clearly show the strong energy dependence of the  $0s_{\frac{1}{2}}$  wave interactions and the almost no energy variation in the  $0p_{\frac{3}{2}}$  wave DPP. The well shapes do not change with energy and the maximal depths are located at 2.0 and 2.2 fm respectively for the  $0s_{\frac{1}{2}}$  and  $0p_{\frac{3}{2}}$  wave results. In the right panel of Fig. 3,  $0d_j$  wave DPPs for the energy of 2.73 MeV are displayed. The results for  $j = \frac{3}{2}$  and  $\frac{5}{2}$  are depicted by the dashed and solid curves respectively, illustrating the spin-orbit attributes formed using the MCAS approach. These variations were found [8] without considering spin depen-

dent scattering data in the determination of the matrix of initial potentials that are input to the MCAS approach. Rather it was the spectrum (bound and resonant) of the compound nucleus ( $^{13}\text{C}$ ) that set the parameterization. Nonetheless spin dependent scattering data were well predicted by this model [8,18].

### 3.1.1 Results using the PB non-local potential

As the non-locality of this model is energy independent, the only question is of what parameter values to use. As there are no parameter values available that best fit relevant data, for simplicity we have chosen those used by Perey and Buck in their calculations with heavier nuclei. As noted, those parameter values suffice since as we seek a qualitative, but not quantitative, comparison of the features of the PB potentials with those found from MCAS. By using  $V_{NL} = -74$  MeV,  $R_{NL} = 2.8$  fm,  $a_{NL} = 0.65$  fm and  $\beta_{NL} = 0.85$  fm, calculations of Eq. (20) gave contour plots shown in the right panel of Fig. 2. The contour lines depict energy spacings of  $10 \text{ MeV}\cdot\text{fm}^{-1}$  with the outermost contour that for  $-0.1 \text{ MeV}\cdot\text{fm}^{-1}$ . The central depths of these partial wave interactions are  $-46.1$ ,  $-36.4$ , and  $-28.7 \text{ MeV}\cdot\text{fm}^{-1}$  for the  $0s_{\frac{1}{2}}$ ,  $0p_{\frac{3}{2}}$ , and  $0d_{\frac{5}{2}}$  waves. Similarities exist between these non-local potentials and those found from low-energy MCAS calculations of the DPP. The depths of the wells for the two studies are comparable, with the depths of the DPP at  $2.73$  MeV being close to the depths of the PB potential for the  $0p_{\frac{3}{2}}$  and  $0d_{\frac{5}{2}}$  waves. The  $0s_{\frac{1}{2}}$  wave MCAS depth is 3 times larger than the PB value however. Nonetheless, it seems that the PB model does have non-locality qualitatively similar to what MCAS yields but the energy independence of the PB model's parameters seems too restrictive.

### 3.1.2 Energy above the first excited state

For energies where more than the elastic channel is open (above  $4.43$  MeV in the case of  $^{12}\text{C}$ ), there is the possibility of flux loss to inelastic scattering. Therefore the DPP become complex. At  $5.0$  MeV in the  $n+^{12}\text{C}$  system, the MCAS method gives the complex DPP for the  $0s_{\frac{1}{2}}$  and  $0p_{\frac{1}{2}}$  waves that are displayed on the top and bottom in Fig. 4 respectively. Contours of the real and imaginary terms are shown on the left and right respectively in each case. The real parts of these potentials at this energy are repulsive with the central strengths of  $5000$  and  $58.8 \text{ MeV}\cdot\text{fm}^{-1}$  for the  $s$  and  $p$  wave cases respectively. The imaginary parts of both potentials are wells with minima of  $-620$  and  $-8.6 \text{ MeV}\cdot\text{fm}^{-1}$  respectively. The contours for the real parts of these potentials are shown for every  $500$  ( $10$ )  $\text{MeV}\cdot\text{fm}^{-1}$  with the  $0s_{\frac{1}{2}}$  ( $0p_{\frac{3}{2}}$ ) wave plots while the imaginary potentials for each indicate changes of  $100$  ( $2$ )  $\text{MeV}\cdot\text{fm}^{-1}$ . Clearly the forms of these potentials, as well as their being complex, have changed markedly from those found for nucleons with energies below that of the

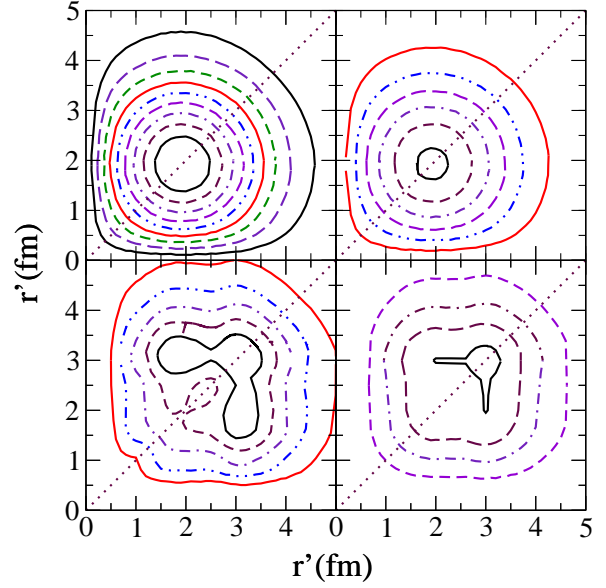


**Fig. 4.** (Color online) Contour plots of the DPP for  $0s_{\frac{1}{2}}$  wave (top) and  $0p_{\frac{1}{2}}$  wave (bottom) at  $5.0$  MeV. The real and imaginary parts are shown on the left and right of each.

threshold of the first excited state in  $^{12}\text{C}$ . There is also distinctively new structure in the  $0p_{\frac{1}{2}}$  DPP.

The new structures of the DPP at  $5.0$  MeV are emphasized with the plots of the diagonal values that are shown in Fig. 5. In the top panel, we show the  $0s_{\frac{1}{2}}$  wave potential along the diagonal. The real part is depicted by the solid curve, the imaginary part by the dashed curve. The bottom section of the diagram contains the real and imaginary components of the  $0p_{\frac{1}{2}}$  wave DPP along the diagonal. Again the real (imaginary) parts are given by the solid (dashed) curves therein. Note that the potential scales are shown in the brackets in each panel. Both DPP have large repulsive real parts with the  $0s_{\frac{1}{2}}$  wave potential being particularly strong. Both also have absorptive imaginary parts. The especial structure of the  $0p_{\frac{1}{2}}$  case, already noted in Fig. 4, is most evident in this plot.

Finally in Figs. 6 and 7, we show the energy variations of the diagonal ( $r = r'$ ) real parts of the DPPs. Those for the  $s_{\frac{1}{2}}$ -,  $d_{\frac{3}{2}}$ -, and  $d_{\frac{5}{2}}$ -waves are depicted in the top, middle, and bottom of Fig. 6 respectively. Note that all of these strengths are given in units of  $\text{MeV}\cdot\text{fm}^{-1}$ . Below the threshold ( $4.43$  MeV) the potentials are purely real and attractive. There is quite strong energy variation in these DPP. At low energies, the DPP have the form of potential wells with minima in the nuclear surface region and those well depths increase with energy, most markedly as the energy approaches a value of about  $4.8$  MeV. For higher energies, those real potentials are strongly repulsive with strength gradually decreasing. Passing through the threshold energy, the DPP acts like a potential wall at or about the nuclear surface. From the specification in



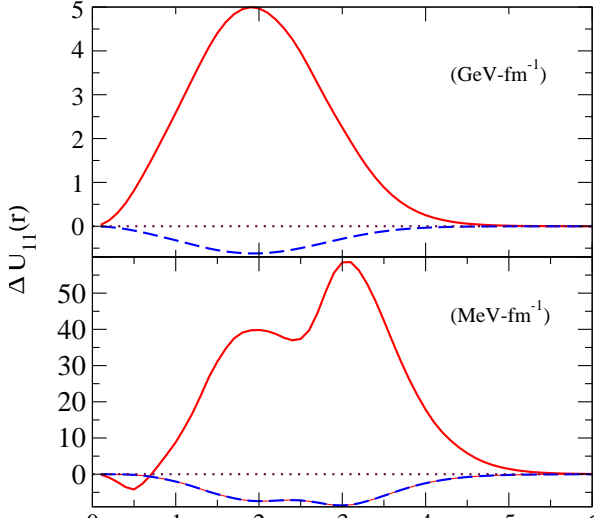


**Fig. 5.** (Color online) The diagonal values of the DPPs obtained using MCAS for 5.0 MeV neutrons scattering from  $^{12}\text{C}$ . The  $0s_{1/2}$  and  $0p_{1/2}$  wave potentials are depicted in the top and bottom sections respectively. Details are given in the text.

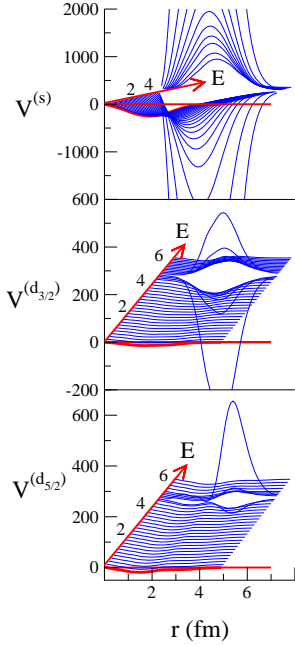


**Fig. 6.** (Color online) Energy variation of the DPP diagonal potentials for the  $s_{1/2}$  wave (top), for the  $d_{3/2}$  wave (middle), and for the  $d_{5/2}$  wave (bottom).

Eqs. (18) and (19), clearly the sharp change in the character of the real parts of these DPP do not necessarily occur at the threshold energy. Depending upon the sturmians and their eigenvalues the scale of change as well as the energy onset can vary with spin-parity of the scattering channel. With the latter, there seems to be a shift to an

energy near 4.8 MeV for each case. However the size of change is very spin-parity dependent.

The diagonal values of the real parts of the DPP for the  $p_{1/2}$  and  $p_{3/2}$  waves are depicted on top and bottom of Fig. 7 respectively. In both, the variation with energy

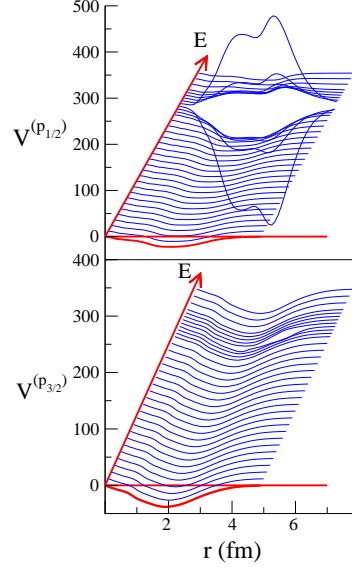


**Fig. 7.** (Color online) Energy variation of the DPP diagonal potentials for the  $p_{1/2}$  wave (top) and for the  $p_{3/2}$  wave (bottom).

across threshold in the  $p_{1/2}$  case is similar to that for the  $d_{3/2}$  wave though a double well aspect is evident now. The threshold effects upon the  $p_{3/2}$  wave DPP show changes but they are much less dramatic than in the DPP for the other partial waves.

### 3.2 Non-locality effects for higher energy data

The cross section and analyzing power for nucleons elastically, and inelastically (to the  $2^+$ , 4.43 MeV state), scattered from  $^{12}\text{C}$  have been calculated using OBDME obtained from a complete  $(0+2)\hbar\omega$  space shell-model calculation [19]. Both WS and harmonic oscillator (HO) functions have been used with those (no-core shell-model) OBDME to calculate the  $^{12}\text{C}$  optical potentials. The transition operators for both elastic and inelastic scattering processes are the medium dependent effective interactions at the relevant energies as described in Sect. 2.2. All of those elements are used in the DWBA98 program [15]. This distorted wave approximation (DWA) code includes exact evaluation of two-nucleon exchange amplitudes that define the knock-out process; amplitudes that are the result of non-local aspects of the reactions since they involve the full nucleon density matrices of the target.

With all details preset, just one calculation is made of both the elastic and inelastic observables for which the process then gives predictions. However, the elements



themselves need assessment of their quality. Much use [1] has established appropriate effective  $NN$  interactions in the nuclear medium as well as of the DWA method (when exchange amplitudes are treated exactly). Thus one need only assess, by other means if possible, the quality of the assumed structure. One excellent way to do that is to use the structure in analyses of electron scattering form factors.

### 3.2.1 An appropriate model of structure

For the specific case we study,  $^{12}\text{C}$ , the longitudinal form factors for elastic and inelastic ( $0^+ \rightarrow 2^+$ ) reactions, and the transverse electric form factor with the latter, have been measured accurately over a reasonable range of momentum transfer values. Those form factors are compared with our calculated ones in Fig. 8. Considering the elastic-

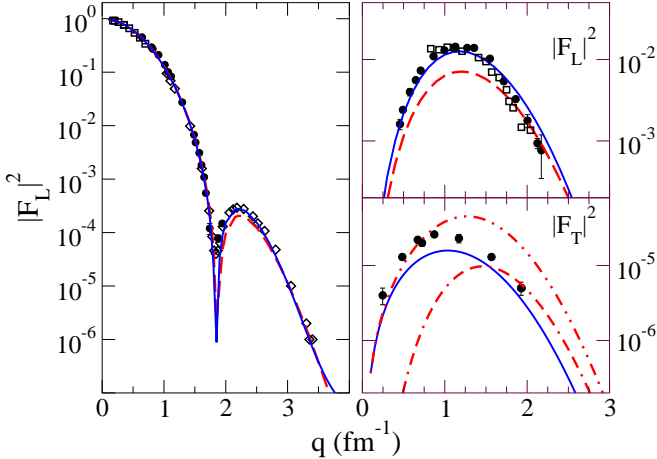


**Fig. 8.** (Color online) Electron scattering form factors for  $^{12}\text{C}$ . The elastic longitudinal form factor is shown in the left panel while the inelastic ones (from excitation of the  $2^+$  (4.43 MeV) state) are shown on the right; longitudinal (top) and transverse electric (bottom). All details are given in the text.

scattering results (left panel) first, the data are those of Jansen *et al.* [20] (squares), of Sick and McCarthy [21] (diamonds), and of Nakada *et al.* [22] (circles). The dashed and solid curves are the results found using WS single particle wave functions with shell occupancies from  $0\hbar\omega$  and  $(0+2)\hbar\omega$  shell-model calculations respectively. The WS potential parameters used to specify the bound-state wave functions and the shell occupancies are given in the review [1]. Similar results were found using HO single-nucleon wave functions when the oscillator length was 1.6 fm. All results agree well with the data though the higher momentum transfer values favor the larger space model of structure. But the form factors for the excitation of the first excited ( $2^+$ ) state given in the right panel of Fig. 8 differentiates more strongly.

In the top part of this panel, we present data and results for the longitudinal electric form factor. The data

displayed by the open squares and filled circles are two sets reported by Flanz *et al.* [23]. They are compared with results found using shell-model transition OBDME from the  $0\hbar\omega$  (dashed curve) and from the  $(0+2)\hbar\omega$  (solid curve) shell-model calculations. Clearly the additional contributions from transitions out of the  $0p$  shell that result in the larger space shell-model study give the extra transition strength required to match observation.

The solid curve shown in the bottom panel is the transverse electric form factor calculated using the  $(0+2)\hbar\omega$  shell-model transition OBDME and WS wave functions. The match to data [23] is good especially when one notes that the separate proton and neutron contributions to this form factor (shown by the dash-double dotted and dot-double dashed curves respectively) have amplitudes that interfere destructively to determine the total result. In the definition of the transition form factor, Siegert operators were used [1] to account for meson exchange current corrections. Thus we have confidence that the no-core  $(0+2)\hbar\omega$  shell model describes well the ground state of  $^{12}\text{C}$  and the excitation of its first excited state, as well as of using those wave functions and OBDME in analyses of nucleon scattering from  $^{12}\text{C}$ . We consider two cases; those for 95 MeV neutrons and for 200 MeV protons.

### 3.2.2 Credibility of the effective interaction

The differential cross sections and analyzing powers for elastic scattering of 200 MeV protons from  $^{12}\text{C}$  that result on using the full non-local optical potentials are compared with data [24] in Fig. 9. Consistent with the results found with the elastic electron scattering form factors, using the Cohen and Kurath [25]  $0p$  shell-model structure makes but little change to the proton elastic-scattering calculations from those displayed. In the left and middle panels in this figure, the solid and long dashed curves display the results obtained by using WS and HO bound-state wave functions. Those panels contain results found from calculations made using  $t$ - (left) and  $g$ - (middle) folding. In  $t$ -folding, the purely free two-nucleon  $t$ -matrices were used as the effective interaction. Thus comparing the results of these two panels shows how important are the medium modifications of the effective  $NN$  interaction. It is evident that  $g$ -folding with WS bound states gives an optical potential from which a differential cross section is obtained that matches the data best. The importance of medium modification in the effective  $NN$  interaction is even more obvious with the analyzing power. The  $g$ -folding results are in much better agreement with data than are the  $t$ -folding ones. However, with this observable as well, there is little to choose between the results obtained using HO and WS bound states for the single-particle bound states of  $^{12}\text{C}$ .

The effect of omitting the exchange amplitudes in defining the elastic scattering are shown in the rightmost panel. Therein the solid curves are the complete  $g$ -folding model results also shown in the middle panel, while the dot-dashed curves are the results when the exchange amplitudes are ignored. Clearly those amplitudes are essential

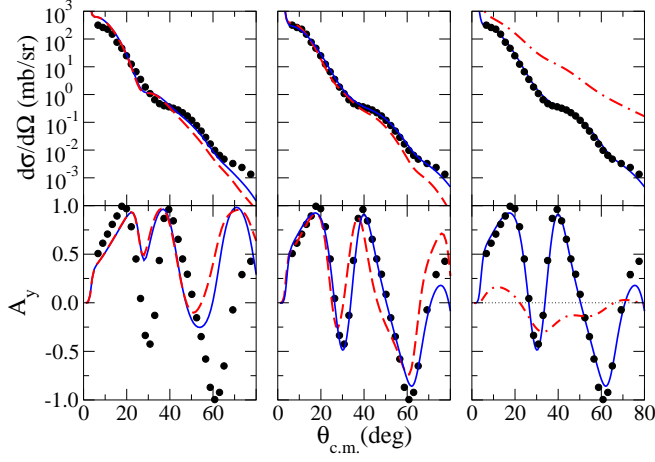


**Fig. 9.** (Color online) 200 MeV proton elastic-scattering cross section (top) and analyzing power (bottom). Data [24] (circles) are compared with the results found using the  $t$ - (left) and  $g$ -folding (middle) optical potentials. The right panel shows the effect of omitting the knock-out amplitudes of the  $g$ -folding potentials. All details are given in the text.

in finding good predictions for both cross sections and analyzing powers. Further discussion is given in the next sub-section.

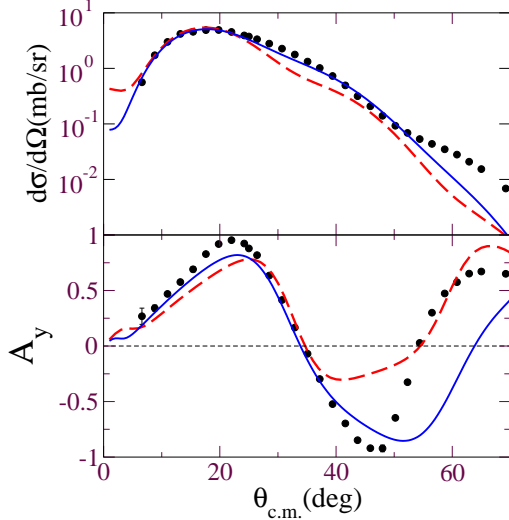


**Fig. 10.** The cross sections and analyzing powers for the inelastic scattering of 200 MeV protons exciting the  $2^+$  4.43 MeV state of  $^{12}\text{C}$ . The solid curves are the complete results and the dashed curves are those found when the medium effects in the effective  $NN$  interaction are omitted.

The quality of the structure and the import of using medium modified effective  $NN$  interactions are confirmed by the results obtained for the inelastic scattering of 200 MeV protons exciting the  $2^+$  (4.43 MeV) state

of  $^{12}\text{C}$ . Data for this reaction are compared with microscopic DWA model results in Fig. 10. Comparison of the two results with the data demonstrates the important role played by medium effects in the  $NN$  interaction in this process. The variation in shapes of results for scattering angles above  $30^\circ$  in the center of mass indicates that. In addition the strength of the scattering is well predicted by the  $(0 + 2)\hbar\omega$  structure model. When a simple  $0\hbar\omega$  spectroscopy was used, this cross section was a factor of four too weak in comparison with the data [1] requiring upward scaling equivalent to an effective charge of  $0.5e$  to match measurement.

### 3.2.3 Effects of the non-local exchange amplitudes

As the non-local nature of the optical potentials formed by  $g$ -folding can be inconvenient, in the past the exchange terms from which those non-localities arise either have been ignored or approximated by a local potential. While the latter approach is the more sensible, we consider what happens by ignoring the exchange terms and so retaining only the “direct” potentials; the leading terms of Eq. (26) i.e. those formed by folding with just the nuclear density and not the full density matrices. By comparing complete with pure direct calculation results, the influence of the exchange terms can be defined.

In the right-most panel of Fig. 9, the differential cross section and analyzing power data (200 MeV elastic proton scattering) are compared with the results of calculations made with the exchange amplitudes included, without any simplification, and with those exchange amplitudes totally excluded. The results are shown by the solid and dot-dashed curves respectively. The difference between the two sets of results is as noteworthy as the quality of agreement between the full calculation results and the data. Such disparity between results with and without the exchange amplitudes persists over a wide range of energies [1]. Of particular note is that the direct and exchange contributions destructively interfere to produce the final result. Also the two amplitudes lead to very different momentum-transfer effects in order that the cross-section results end up in the agreement with data found.

### 3.2.4 Neutron scattering and effects of exchange amplitudes

The cross section from the elastic scattering of 95 MeV neutrons from  $^{12}\text{C}$  has been measured recently [26] and these data are shown by the filled circles in the left panel of Fig. 11. Older data taken at 40.3 MeV [27] are shown therein by the filled squares. The middle and left panels show the results of 95 MeV neutron scattering elastic (top) and inelastic, to the  $2^+$  (4.43 MeV) state, (bottom) cross section and analyzing powers respectively. The solid curves depict the results obtained using the complete  $g$ -folding model with WS wave functions and orbit occupancies from the  $(0 + 2)\hbar\omega$  shell model. The dashed curves depict what result on omitting the exchange amplitudes.

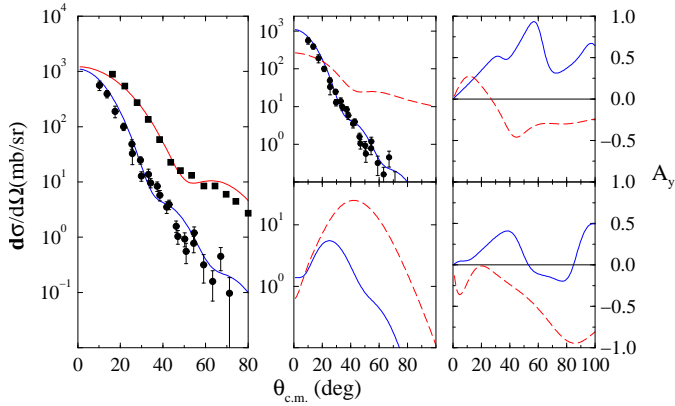


**Fig. 11.** In the left panel are the cross sections for 40.3 MeV and for 95 MeV neutrons scattered elastically from  $^{12}\text{C}$ . In the middle panel are the cross sections for elastic (top) and inelastic scattering (bottom) found with (solid) and without (dashed) the knock-out amplitudes. The right panel are the analyzing powers associated with them. Details are given in the text.

At both energies, treating the exchange terms without approximation to get the optical potentials gave cross sections in very good agreement with the data. The contrast of these results with those given by the calculations made omitting the exchange amplitudes is dramatic. The structure of the cross sections and analyzing powers are radically changed as is the predicted magnitude of the inelastic excitation. These variations are similar to those noted above with the (elastic) scattering of 200 MeV protons.

Of particular import is that, at all three energies considered, the role of the exchange (non-locality) in evaluations of both the elastic and inelastic-scattering cross sections is of destructive interference. Such interference makes representation of the non-local interactions by an equivalent local interaction suspect. Also the effects in the analyzing powers are dramatic and it must be remembered that those observables involve the cross section as a denominator. A fit to any analyzing power then without first having a good cross section prediction is but fortuitous.

## 4 Conclusions

The origins and effects of non-localities in the  $NA$  optical potential have been studied with separate methods of data analysis most appropriate for low and for medium projectile energies. The scattering of nucleons from  $^{12}\text{C}$  have been considered.

For low energies (0 to  $\sim 6$  MeV) the MCAS method was used to describe  $n+^{12}\text{C}$  scattering. With that theory the origins of non-localities in optical potentials due to antisymmetry of projectiles with target nucleons and the dynamic polarization potential representation of channel coupling were detailed. A collective model was used to specify the matrix of interaction potentials that were the

basic input to the approach. The resulting DPP is strongly non-local with also strong  $l$ -dependence. At the energies studied the dominant term is that of  $0s_{\frac{1}{2}}$  wave interaction whose character varies markedly to carry the resonance features of the full coupled-channel results.

At medium energies, the  $g$ -folding method with no-core, large space, Shell model wave functions and the Melbourne force, a complex effective  $NN$  interaction that is density and energy dependent, was used. That approach attributes the effective channel coupling to be with an effective infinity of target states in which one or more nucleons are in the continuum. It is equivalent to using the KMT theory but with the effective interaction between the projectile and each and every target nucleon being modified by the medium. The cross sections obtained when compared with data, established that one cannot ignore either medium modification of the  $NN$  interaction or the exchange (knock-out) contributions in forming optical potentials. That is observed strongly also when the DWA is used to evaluate observables from inelastic scattering. The complete  $g$ -folding process makes the optical potential complex, energy dependent, and non-local. But, as the  $g$ -matrices are strongly medium dependent, the non-local attributes of the optical potentials themselves are not easily displayed. Indeed in the DWBA98 code such are not explicitly evaluated in finding solutions of the integro-differential equations from which phase shifts are specified [1]. The import of that non-locality is evident however in the comparisons made with data at many energies and with and without the exchange terms included in the calculations of the cross sections and analyzing powers. Clearly, any localization of the non-local potential is approximating a most important factor in data analysis.

## acknowledgments

This research was supported by the Italian MIUR-PRIN Project “Fisica Teorica del Nucleo e dei Sistemi a Più Corpi”, by the Natural Sciences and Engineering Research Council (NSERC), Canada, and by the National Research Foundation of South Africa.

## References

1. K. Amos, P. J. Dortmans, H. V. von Geramb, S. Karataglidis, and J. Raynal, *Adv. in Nucl. Phys.* **25**, (2000); and references cited therein.
2. H. Feshbach, *Theoretical Nuclear Physics: Nuclear Reactions*, (Wiley, 1992).
3. F. G. Perey and B. Buck, *Nucl. Phys.* **32**, (1962) 353.
4. L. Canton, G. Pisent, J. P. Svenne, D. van der Knijff, K. Amos, and S. Karataglidis, *Phys. Rev. Lett.* **94**, (2005) 122503.
5. A. K. Kerman, H. McManus, and R. M. Thaler, *Ann. Phys. (N.Y.)* **8**, (1959) 551.
6. H. V. von Geramb, K. Amos, R. Sprickmann, K. T. Knöpfle, M. Rogge, D. Ingham, and C. Mayer-Böricke, *Phys. Rev. C* **12**, (1975) 1697.

7. K. Amos, S. Karataglidis, D. van der Knijff, L. Canton, G. Pisent, and J. P. Svenne, *Phys. Rev. C* **72**, (2005) 065604.
8. K. Amos, L. Canton, G. Pisent, J. P. Svenne, and D. van der Knijff, *Nucl. Phys.* **A728**, (2003) 65.
9. G. Pisent, J. P. Svenne, L. Canton, K. Amos, S. Karataglidis, and D. van der Knijff, *Phys. Rev. C* **72**, (2005) 014601.
10. G. Cattapan, L. Canton, and G. Pisent, *Phys. Rev. C* **43**, (1991) 1395.
11. G. Cattapan, L. Canton, and G. Pisent, *Phys. Lett.* **B 240**, (1990) 1.
12. L. Canton, Y. Hahn, and G. Pisent, *Phys. Rev. C* **43**, (1991) 2441.
13. H. A. Bethe, B. H. Brandow, and A. G. Petschek, *Phys. Rev.* **129**, (1963) 225.
14. H. F. Arellano, F. A. Brieva, M. Sander, and H. V. von Geramb, *Phys. Rev. C* **54**, (1996) 2570.
15. J. Raynal, *computer program DWBA98*, NEA 1209/05, (1998).
16. S. Pearlman, *ENDF/HE-VI Mat-625*, BNL-48035, (1993).
17. *Computer Index of Neutron Data (CINDA)* IAEA - NDS database (2005).
18. J. P. Svenne, K. Amos, S. Karataglidis, D. van der Knijff, L. Canton, and G. Pisent, *Phys. Rev. C* **73**, (2006) 027601.
19. S. Karataglidis, P. J. Dortmans, K. Amos, and R. de Swiniarski, *Phys. Rev. C* **52**, (1995) 861.
20. J. A. Jansen, R. Th. Peerdeman, and C. de Vries, *Nucl. Phys.* **A188**, (1972) 337.
21. I. Sick and J. S. McCarthy, *Nucl. Phys.* **A150**, (1970) 631.
22. A. Nakada, Y. Torizuka, and Y. Horikawa, *Phys. Rev. Lett.* **27**, (1971) 745, 1102.
23. J. B. Flanz, R. S. Hicks, R. A. Lindgren, G. A. Peterson, A. Hotta, B. Parker, and R. C. York, *Phys. Rev. Lett.* **41**, (1978) 1642.
24. J. R. Comfort, G. L. Moake, C. C. Foster, P. Schwandt, and W. G. Love, *Phys. Rev. C* **26**, (1982) 1800.
25. S. Cohen and D. Kurath, *Nucl. Phys.* **73**, (1965) 1.
26. J. Klug *et al.* *Phys. Rev. C* **67**, (2003) 031601.
27. J. S. Winfield, S. M. Austin, R. P. DeVito, U. E. Berg, Z. Chen, and W. S. Sterrenburg, *Phys. Rev. C* **33**, (1986) 1.